OXFORD CDE

Journal of Computational Design and Engineering, 2022, **9**, 1549–1564

DOI: 10.1093/jcde/qwac074
Advance access publication date: 1 August 2022
Research Article

Learning-based catheter and guidewire-driven autonomous vascular intervention robotic system for reduced repulsive force

Hwa-Seob Song[1], Byung-Ju Yi[2], Jong Yun Won[3,*] and Jaehong Woo[4,*]

[1]Research Institute Engineering and Technology, Hanyang University, Hanyangdaehak-ro 55, Sangnok-gu, Ansan 15588, Republic of Korea
[2]School of Electrical Engineering, Hanyang University, Hanyangdaehak-ro 55, Sangnok-gu, Ansan 15588, Republic of Korea
[3]Department of Radiology, Severance Hospital, Research Institute of Radiological Science, Yonsei University College of Medicine, Yonsei-ro 50-1, Seodaemun-gu, Seoul 03722, Republic of Korea
[4]Department of Robotics and Convergence, Hanyang University, Hanyangdaehak-ro 55, Sangnok-gu, Ansan 15588, Republic of Korea
*Corresponding author. E-mail: JYWON@yuhs.ac (JYW); jokers12@hanyang.ac.kr (JW)

Abstract

Manual vascular interventional radiology (VIR) procedures have been performed under radiation exposure conditions, and many commercial master–slave VIR robot systems have recently been developed to overcome this issue. However, master–slave VIR robot systems still have limitations. The operator must reside near the master device and control the slave robot using only the master device. In addition, the operator must simultaneously process the recognition of the surgical tool from the X-ray image while operating the master device. To overcome the limitations of master–slave VIR robot systems, we propose an autonomous VIR robot system with a deep learning algorithm that excludes the master device. The proposed autonomous VIR robot with a deep learning algorithm drives surgical tools to the target blood vessel location while simultaneously performing surgical tool recognition. The proposed autonomous VIR robot system detects the location of the surgical tool based on a supervised learning algorithm, and controls the surgical tools based on a reinforcement-learning algorithm. Experiments are conducted using two types of vascular phantoms to verify the effectiveness of the proposed autonomous VIR robot system. The experimental results of the vascular phantom show a comparison between the master–slave VIR robot system and the proposed autonomous VIR robot system in terms of the repulsive force, task completion time, and success rate during the operation. The proposed autonomous VIR robot system is shown to exhibit a significant reduction in repulsive force and a 96% success ratio based on a vascular phantom.

Keywords: reinforcement learning, supervised learning, vascular intervention, autonomous system, surgical robot

List of symbols

AI:	Artificial intelligence
B :	Number of bounding boxes
C_i :	Confidence score of the box j in cell i
DOF :	Degree of freedom
F/T :	Force/torque
IOU:	Intersection over union
k_1, k_2, k_3, k_4 :	Weight of reward function
$p_i(c)$:	Coordinates of the conditional class probability for class c in cell i
R :	Reward value
S :	Grid size of image
VIR :	Vascular interventional radiology
w_i, h_i :	Bounding box width and height
YOLO :	You Only Look Once
x_i, y_i :	Coordinate of ith bounding box center inside cell
X_{go}, Y_{go} :	Goal position in reinforcement learning environment
X_{ca}, Y_{ca} :	Catheter position in reinforcement learning environment
X_{gi}, Y_{gi} :	Guidewire position in reinforcement learning environment
1_i^{obj} :	1 if an object appears in cell i; otherwise 0
1_{ij}^{obj} :	1 if the jth boundary box in cell i is responsible for detecting object; otherwise 0
1_{ij}^{noobj} :	1 if the jth boundary box in cell i is not responsible for detecting object; otherwise 0
λ_{coord} :	Balancing parameter for balancing the loss
λ_{noobj} :	Balancing parameter for bounding boxes with and without objects
$\wedge$:	Prediction result of neural network

1 Introduction

The first reported attempts to perform vascular treatment employed an open surgical approach because vascular interventional radiology (VIR) was initially focused on the reconstruction of blood vessels (Friedman, 2005). The discovery of X-rays and contrast agents enabled VIR procedures to observe the inside of the body without opening the body. Owing to these advances, the VIR procedure has evolved into a minimally invasive surgery for many types of surgery. The VIR procedure was developed as a percutaneous treatment method that uses a variety of devices such

Received: March 29, 2022. **Revised:** July 25, 2022. **Accepted:** July 26, 2022

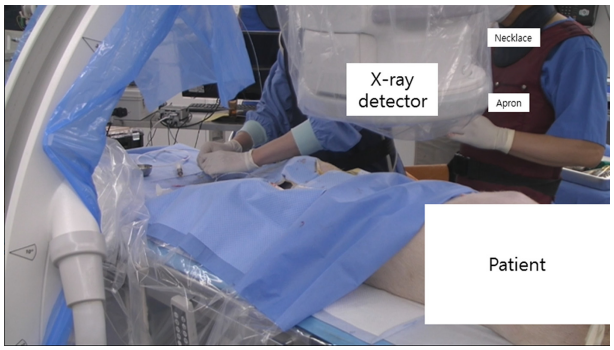

Figure 1: Condition of conventional VIR procedure.

as catheters and guidewires with minimal incisions. Recently, the VIR procedure has been widely used not only for vascular system treatment, but also for embolization to treat cancer (Wáng *et al.*, 2015). Angiography and angioplasty are the most commonly performed VIR procedures worldwide (Miller *et al.*, 2003; Goni *et al.*, 2005; Vano *et al.*, 2006; Pantos *et al.*, 2009; Efstathopoulos *et al.*, 2011; Mohapatra *et al.*, 2013). With the advancement of the VIR procedure in the field of minimally invasive surgery, the number of procedures undertaken has also shown explosive growth (Anderson *et al.*, 2004; Schanzer *et al.*, 2009). While the number of VIR procedures is increasing, the number of vascular surgeons is decreasing (Satiani *et al.*, 2009). From the patient perspective, the absence of a doctor to apply VIR makes it difficult to manage diseases that require emergency surgery. In the case of acute ischemic stroke and acute myocardial infarction, the mortality rate depends on the time of vascular intervention after disease onset (Boersma *et al.*, 1996; Chareonthaitawee *et al.*, 2000; Satiani *et al.*, 2009; Advani *et al.*, 2017; Mulder *et al.*, 2018). In addition, the number of vascular interventional procedures performed is significant from the doctor's perspective, as there are side effects due to cumulative radiation exposure. A typical side effect of radiation exposure is skin damage (Weerakkody *et al.*, 2008). To prevent such side effects, the International Commission on Radiological Protection regulates radiation dose limits for occupational exposure to radiation. According to Publication 103 (Wrixon, 2008), the actual dose limit for radiation workers is 50 mSv/year. Unfortunately, both patients and doctors are exposed to large amounts of X-ray radiation during conventional VIR procedures. In conventional VIR procedures, doctors wear protective gear to prevent radiation exposure, as shown in Fig. 1. However, radiation workers may experience physical fatigue owing to the apron's weight. In addition, radiation protection gloves are rarely used during surgical procedures in operating theatres. Consequently, hands are still exposed to high doses (Efstathopoulos *et al.*, 2011). To overcome these limitations of conventional VIR procedures, many types of remote master–slave VIR robot systems have been developed to reduce the cumulative radiation exposure of doctors while performing VIR procedures.

Hansen Medical Co. developed the Magellan and Sensei robot systems (Duran *et al.*, 2014). The Magellan robot system uses 6 French robot catheter and a 0.035-inch guidewire for various VIR procedures. The operator uses the master console of the Magellan robot system to perform VIR at a certain distance from the X-ray source. The Sensei robot system also has robotic catheter force sensing. The sensed force provides haptic feedback to the master device of the master console through vibrations, allowing the doctor to feel the force generated by the catheter.

The Corindus developed the CorPath GRX VIR robotic system (Britz *et al.*, 2019), which also controls the catheter and guidewire by using the master device of the master console. As CorPath GRX is also a master–slave robot system, the results of a clinical trial showed that radiation exposure to doctors reduced by approximately 97%, and radiation exposure to patients decreased by approximately 20% (Mahmud *et al.*, 2020; Patel *et al.*, 2020). In addition, the performance of the CorPath GRX robot system was evaluated and announced to be equal to or better than that in cases involving manual procedures (Granada *et al.*, 2011).

The Amigo is also based on a master–slave robot system (Khan *et al.*, 2013). Similar to other VIR robot systems, the Amigo robot system can reduce the radiation exposure of doctors. However, because the catheter does not have force-sensing ability, vascular perforation may occur because of the insertion force of the catheter during the VIR procedure. Previously, commercial VIR robot systems focused primarily on the accuracy of the VIR procedure and the reduction of radiation exposure.

The latest research aimed to solve the disadvantages of conventional surgery using the developed medical robot, and attempted a new methodology. Recent developments in artificial intelligence (AI) have seen its application in the fields of surgical robots and medicine. Thus, many surgical robots and AI algorithm researches are being conducted. There are several examples of previous studies on the application of AI in the vascular intervention field. Various studies have been conducted based on the reinforcement learning algorithm for catheter and guidewire insertion to the target point, which is a procedure for VIR after insertion of the introduction sheath. Behr *et al.* (2019) and Karstensen *et al.* (2020) proposed a study to control a guidewire to a random vascular phantom target point by training a deep Q-network and a deep deterministic policy gradient agent. Furthermore, Karstensen *et al.* (2022) conducted an experiment based on a porcine liver model to verify learning-based guidewire control without human-generated data . By adding experience replay and human demonstration to the automatic guidewire-driven reinforcement learning algorithm, Behr *et al.* proved the results of shortening the learning time and increasing the success rate by performing a two-dimensional (2D) phantom-based experiment. Also, Kweon *et al.* (2021) evaluated guidewire navigation experiments with deep Q-learning from human demonstration and transfer learning to validate the framework in a three-dimensional (3D) coronary artery model. On the other hand, there are also previous studies on autonomous catheter-driven. Chi *et al.* (2020) proposed an autonomous driving catheter with a generative adversarial imitation learning algorithm. Chi *et al.* measured the force generated between the blood vessel and catheter during catheter insertion using a force sensor. Phantom experiments verified that the proposed automated robot system minimized the force exerted against the catheter. In addition, You *et al.* presented the result of increasing the success rate of autonomous catheter-driven in a 3D heart model by applying the simulation learning results and randomization noise (You *et al.*, 2019).

However, the previous autonomous VIR robots were limited to operating with only a catheter or guidewire. Robots with only catheter or guidewire drives may be suitable for interventions targeting large vessels, such as the cardiovascular system, but not for vessels with tortuous and angulated (Li *et al.*, 2018). For this reason, Corindus developed the Corpath GRX to treat complex coronary lesions by adding a catheter-forward motion that was not presented in the Corpath 200 (Crinnion *et al.*, 2022). Therefore, to achieve autonomous VIR in general blood vessels, both the catheter and guidewire are required. In addition, because there is

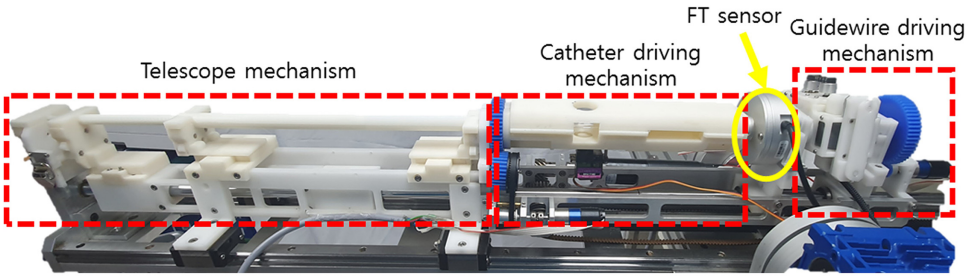

Figure 2: Four-DOF VIR slave robot mechanism and module description.

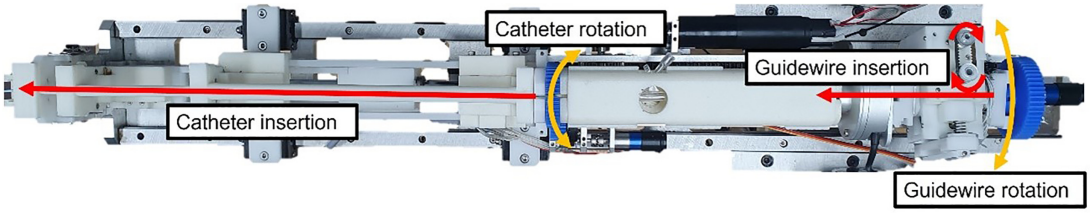

Figure 3: Catheter insertion/rotation and guidewire insertion/rotation motions of VIR slave robot.

no doctor's intervention in autonomous VIR procedures, there is a threat of vascular perforation owing to the excessive operation of the surgical tool of the robot. Thus, it is essential to measure the force of the catheter.

To overcome the limitations of the developed autonomous VIR robot system, we propose an autonomous VIR robot system based on a deep-learning algorithm integrated with a force/torque (F/T) sensor to measure the repulsive force of the catheter. In this research, a previously developed five degree-of-freedom (DOF) slave robot (Cha *et al.*, 2016, 2017; Woo *et al.*, 2019) was used, and a reinforcement learning algorithm was implemented for autonomous catheter and guidewire manipulation. In addition, the catheter and guidewire position-tracking algorithm was implemented based on You Only Look Once (YOLO). To reduce the possibility of vascular perforation, an F/T sensor is mounted on the VIR robot to measure the repulsive force between the vessel wall and catheter. The objectives of the reinforcement learning algorithm applied in this study are to automatically drive the catheter and guidewire from the starting point of the target blood vessel and to minimize the repulsive force of the catheter. The results obtained for the proposed autonomous VIR robot system verified the effectiveness of the autonomous VIR procedure and minimized the repulsive force of the catheter based on phantom experiments.

2 Four-DOF VIR Slave Robot

The four-DOF VIR slave robot is presented in Fig. 2. The robot for the VIR procedure (Cha *et al.*, 2016; Woo *et al.*, 2019) was a modified version from the four-DOF robot (Cha *et al.*, 2017). The four-DOF VIR robot is equipped with an F/T sensor (ROBOTUS, RFT60-HA01) to measure the force between the catheter and blood vessel (Cha *et al.*, 2017).

The four-DOF VIR robot has catheter insertion/rotation and guidewire insertion/rotation motions, as shown in Fig. 3.

2.1 Conventional master–slave VIR robot system

Previously, VIR robot systems were mainly developed as master–slave systems (Khan *et al.*, 2013; Duran *et al.*, 2014; Cha *et al.*, 2016, 2017; Britz *et al.*, 2019; Woo *et al.*, 2019; Bassil *et al.*, 2020; Jeong *et al.*, 2020; Mahmud *et al.*, 2020; Patel *et al.*, 2020; Harel, 2021). Conventional VIR master–slave robot systems have focused on reducing radiation exposure and the accurate manipulation of surgical tools. The advantage is that the operator can significantly reduce radiation exposure using the master device in front of the master console without the need to be next to the patient (near the X-ray) in order to control the VIR tools installed on the slave robot, as shown in Fig. 4. The haptic feedback function of the conventional master–slave VIR robot system is also important for reducing the task time and possibility of vascular perforation. Accordingly, Tahir *et al.* presented the effectiveness of haptic feedback during coronary interventions (Tahir *et al.*, 2022).

To drive the master–slave VIR robot system, an operator should participate in the operation of the master device. The operator observes the real-time medical image screen to recognize the current status of the procedure, and simultaneously controls the surgical tool to enter the target vessel using the master device. The workflow of the conventional master–slave VIR robot system is shown in Fig. 5.

However, master–slave VIR robot systems still have limitations. Although the VIR master–slave robot system reduced the mental/physical burden compared with the manual VIR procedure, the robot system still requires much work from the operator's perspective. Further, in the case of teleoperation, a communication delay still exists, which makes the operation difficult (Lum *et al.*, 2009). Therefore, in the next section, we propose an autonomous VIR robot system to prevent the operator from focusing on a large amount of work and to eliminate difficult situations during teleoperation due to communication delays.

2.2 Proposed autonomous VIR robot system

In this study, we propose an autonomous VIR robot system by improving the slave robot proposed by Woo *et al.* (2019), which was our previous study. The workflow of the proposed autonomous VIR robot system is illustrated in Fig. 6, which also shows the difference between the conventional master–slave type VIR robot system and the autonomous VIR robot system.

With the autonomous VIR robot, the operator is involved only in setting the target position, and is not involved in the subse-

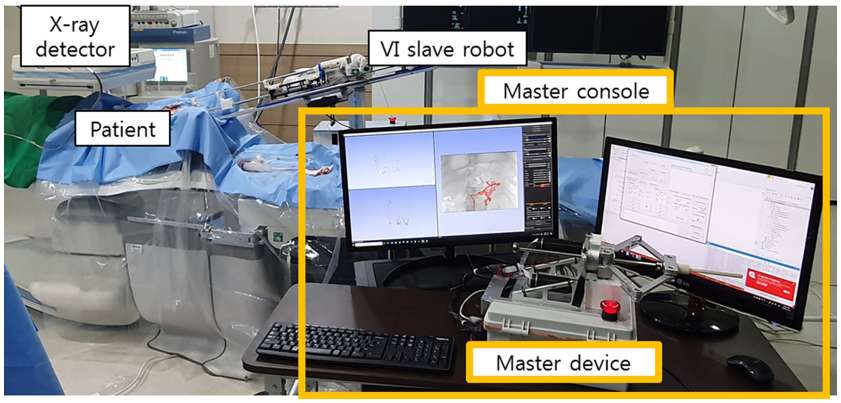

Figure 4: The setting condition of the conventional master–slave VIR robot system in the operating theater.

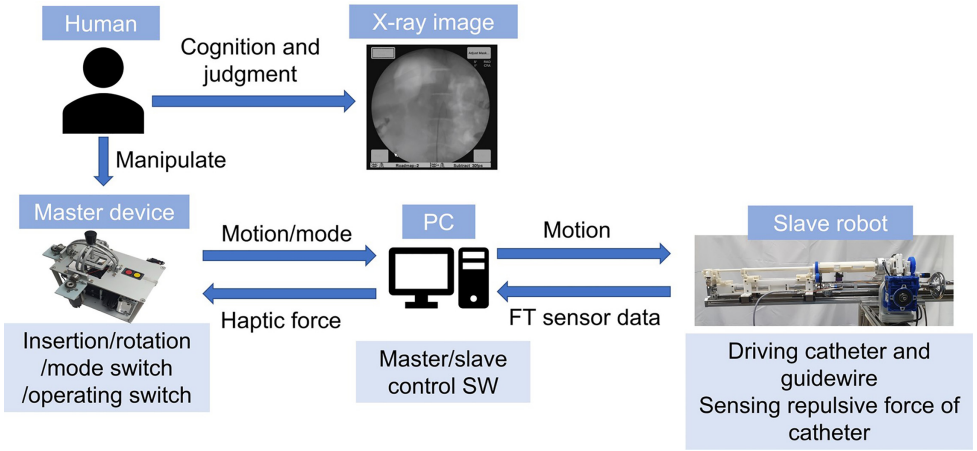

Figure 5: Description and workflow of the conventional master–slave VIR robot system.

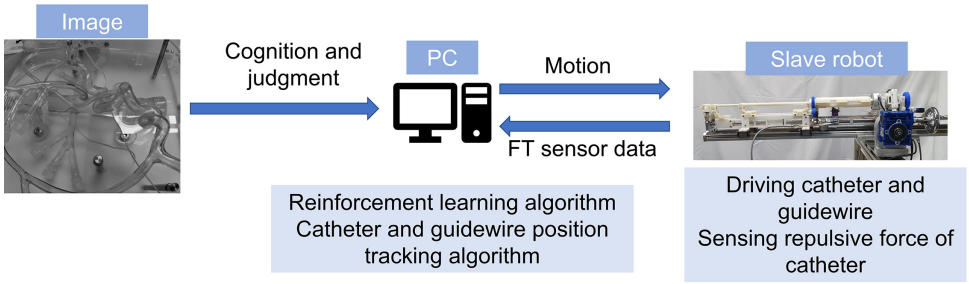

Figure 6: Description of the proposed autonomous VIR robot system workflow.

quent VIR procedure. The first goal of the autonomous VIR robot aims to control the robot to reach the VIR tool in the target vessel. The second goal is to minimize the repulsive force based on the reinforcement learning.

3 AI Algorithms for Autonomous VIR Robot

The algorithms of the autonomous VIR robot system consist of a reinforcement learning algorithm to control surgical tools and a supervised learning algorithm to track the position of surgical tools using camera images. First, the catheter and guidewire position-tracking algorithm was implemented based on the YOLO algorithm. The catheter and guidewire position-tracking algorithm draws a square box to indicate the position of the catheter and guidewire in the output image from the camera. This algorithm was designed to enable the accurate positioning of the surgical tools. The results of the tracking algorithm are used in the reinforcement algorithm to determine the state of the surgical tools. Second, the reinforcement learning algorithm aims to control the surgical tools. The reinforcement learning algorithm learns how the robot is controlled to approach the position of the target vessel based on the position information of the surgical tools received by the catheter and guidewire position-tracking algorithm.

A block diagram of the autonomous VIR robot software is shown in Fig. 7. The AI algorithms are implemented based on Python. The results of the surgical tools position-tracking algorithm is transferred to the reinforcement learning algorithm. The reinforcement-learning algorithm determines the state, action,

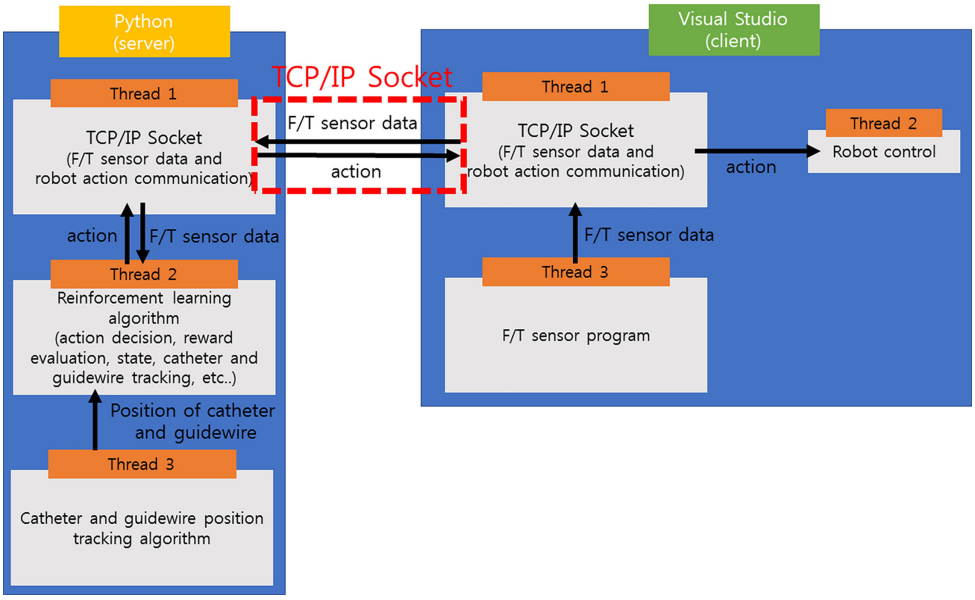

Figure 7: Description of the proposed autonomous VIR robot system algorithms.

and reward values based on the surgical tools' position information. Then, the determined action is transmitted to the robot control program through TCP/IP socket communication. The robot control program is implemented based on C++ visual studio. The robot control program controls the robot based on the action determined by the reinforcement learning algorithm. In addition, the repulsive force measured by the F/T sensor is transmitted to the reinforcement-learning algorithm. This process was repeated until the surgical tools reached the target position.

3.1 Catheter and guidewire position-tracking algorithm

This section describes the catheter and guidewire position-tracking algorithm, which is one of the two core algorithms applied to the autonomous VIR robot system. In previous studies, various methods were used for the position-tracking of surgical tools. Chi *et al.* (2018) conducted a previous study in which an electromagnetic sensor was applied to track the position of a catheter. In a previous study, the model-based catheter tracking algorithm showed a tracking speed of 23 frames per s (Ma *et al.*, 2013). Also, a convolution neural network (CNN) was applied for guidewire position-tracking (Kweon *et al.*, 2021; Karstensen *et al.*, 2022).

However, if the electromagnetic sensor is coupled with a catheter to recognize a surgical tool's position, it is unsuitable for insertion into the body. The CNN-based surgical tool position-tracking within the image has a less physical burden on blood vessels, and it is feasible to track the position of one tool and two or more tools simultaneously. In this study, we applied an AI neural network to track the position of two or more surgical tools faster without applying a hidden Markov model or Bayesian information criterion that requires a small amount of computation.

An AI neural network called YOLO was applied to the position-tracking algorithm of the surgical tools. The YOLO algorithm was developed for object recognition (Redmon *et al.*, 2016). The YOLO algorithm redefines the concept of object recognition in an image, from a multi-task to regression. YOLO predicts the bounding box and class probability for the entire image using a single neural network with only one computation. The YOLO algorithm in this study shows a fast computation time of about 35 frames per s. Additionally, if sufficient training data exists for the additional surgical tool, the YOLO algorithm is a viable method for tracking additional surgical tools. The bounding box is a rectangular box that wraps around an object to indicate its location. The class probability is the probability that the object enclosed by the bounding box corresponds to a particular class. YOLO is characterized by an end-to-end format and fast frame processing speed because the object detection pipeline is composed of one neural network. Table 1 shows the neural network structure used for position tracking of the catheter and guidewire employed in this research.

Table 1: Neural network structure used for position tracking of the catheter and guidewire.

Type	Filters	Size/stride	Output
Convolutional	32	3 × 3/1	608 × 608
Maxpool		2 × 2/2	304 × 304
Convolutional	64	3 × 3/1	304 × 304
Maxpool		2 × 2/2	152 × 152
Convolutional	128	3 × 3/1	152 × 152
Convolutional	64	1 × 1/1	152 × 152
Convolutional	128	3 × 3/1	152 × 152
Maxpool		2 × 2/2	76 × 76
Convolutional	256	3 × 3/1	76 × 76
Convolutional	128	1 × 1/1	76 × 76
Convolutional	256	3 × 3/1	76 × 76
Maxpool		2 × 2/2	76 × 76
Convolutional	512	3 × 3/1	38 × 38
Convolutional	256	1 × 1/1	38 × 38
Convolutional	512	3 × 3/1	38 × 38
Convolutional	256	1 × 1/1	38 × 38
Convolutional	512	3 × 3/1	38 × 38
Maxpool		2 × 2/2	19 × 19
Convolutional	1024	3 × 3/1	19 × 19
Convolutional	512	1 × 1/1	19 × 19
Convolutional	1024	3 × 3/1	19 × 19
Convolutional	512	1 × 1/1	19 × 19
Convolutional	1024	3 × 3/1	19 × 19
Convolutional	35	1 × 1/1	19 × 19

3.2 Preparation of training data for catheter and guidewire position-tracking algorithm

In this study, we are using an RGB camera to track surgical tools in vascular phantom environments. The X-rays used in the VIR procedure is a grayscale images. Therefore, grayscale images from the RGB camera were used as training data for the catheter and guidewire position-tracking neural network. YOLO is a supervised learning method. Thus, we have prepared image boundary box labeling data using the software LabelImg. A bounding-box label was conducted for the catheter and guidewire. The grayscale images and label data were used as a pair of training inputs, with each input dataset having paired grayscale images of the surgical tools and bounding box labels, as shown in Fig. 8.

A total of 182 images were collected as training data by inserting a catheter and guidewire into the vascular phantom. Owing to the limited amount of training data, 10 augmentation datasets were generated for every part of the training data image, resulting in a total of 2002 sets of image data. The data augmentation applied in this research included a rotation range between −9 and 9°, a change in width shift between −60 and +60 pixels, a change in height shift between −60 and 60 pixels, and zoom change between −5 and 5% of the image size.

3.3 Training phase of the catheter and guidewire position-tracking algorithm

The training phase involves learning the 2002 images of surgical tools and boundary-box labels. A few concepts will be introduced before explaining the loss function of the YOLO neural network used in this research. The YOLO network used in this study is converted into an image with a 19 × 19 grid as the output after the image passed through the neural network. Each grid cell has a confidence score, bounding boxes, and conditional class probabilities. The expressions for the confidence score and conditional class probability are as follow:

$$\text{Confidence score} = Pr(Object) * \text{IOU}_{\text{pred}}^{\text{truth}} \tag{1}$$

$$\text{Confidencal class probability} = Pr(Class_i|Object), \tag{2}$$

where IOU stands for intersection over union. IOU is defined as follows:

$$\text{IOU} = \frac{\text{Overlapping region}}{\text{Combined region}}. \tag{3}$$

The class-specific confidence score is obtained by multiplying the conditional class probability by the confidence score of the bounding box. The class-specific confidence score is calculated as follows:

$$\begin{aligned}&\text{Class specific confidence score}\\ &= \text{Conditional class probability} * \text{Confidence score}\\ &= Pr(Class_i|Object) * Pr(Object) * \text{IOU}_{\text{pred}}^{\text{truth}}\\ &= Pr(Class_i) * \text{IOU}_{\text{pred}}^{\text{truth}}.\end{aligned} \tag{4}$$

The loss function of the YOLO neural network is as follows:

$$\lambda_{\text{coord}} \sum_{i=0}^{S^2} \sum_{j=0}^{B} 1_{ij}^{\text{obj}} \left[(x_i - \hat{x}_i)^2 - (y_i - \hat{y}_i)^2 \right] \tag{5}$$

$$+ \lambda_{\text{coord}} \sum_{i=0}^{S^2} \sum_{j=0}^{B} 1_{ij}^{\text{obj}} \left[\left(\sqrt{w_i} - \sqrt{\hat{w}_i} \right)^2 - \left(\sqrt{h_i} - \sqrt{\hat{h}_i} \right)^2 \right] \tag{6}$$

$$+ \sum_{i=0}^{S^2} \sum_{j=0}^{B} 1_{ij}^{\text{obj}} (C_i - \hat{C}_i)^2 \tag{7}$$

$$+ \lambda_{\text{noobj}} \sum_{i=0}^{S^2} \sum_{j=0}^{B} 1_{ij}^{\text{noobj}} (C_i - \hat{C}_i)^2 \tag{8}$$

$$+ \sum_{i=0}^{S^2} 1_i^{\text{obj}} \sum_{c \in \text{classes}} [p_i(c) - \hat{p}_i(c)]^2, \tag{9}$$

where S denotes the grid, B represents the number of bounding boxes, and C represents the number of conditional class probabilities. Each bounding box is composed of x, y, w, and h confidence. x and y refer to the midpoints of the bounding box. When calculating the loss function, it is used as a relative value in the grid cell range. w and h are the relative values of the width and height of the entire image. For example, if y is at the top of the grid cell, $y = 0$; if x is at the middle of the grid cell, $x = 0.5$; and if the height of the bounding box is half the image, $h = 0.5$. There are several assumptions to be made before calculating the loss function of Equations (5–9). First, among the several bounding boxes of the grid cell, the bounding box with the highest IOU and the ground-truth box is determined as a predictor. According to the first criterion, the symbols 1_i^{obj}, 1_{ij}^{noobj}, and 1_{ij}^{obj} are used. 1_{ij}^{obj} is the predictor bounding box j of i in the grid cell in which the object exists. 1_{ij}^{obj} is the grid cell i where the object exists. Thus, Equation (5) represents the loss of x and y for the predictor bounding box j of the grid cell i where the object exists. Equation (6) shows the loss of w and h for the predictor bounding box j of the grid cell i in which the object exists. Equation (7) presents the loss of the confidence score for the predictor bounding box j of the grid cell i where the object exists. Equation (8) shows the loss of confidence score for the predictor bounding box j of the grid cell i where the object does not exist. Finally, Equation (9) represents the loss of the conditional class probability for grid cell i where the object exists. If the object determined using the neural network is correct, $p_i(c) = 1$; otherwise, $p_i(c) = 0$. λ_{coord} denotes the balancing parameter for the loss of coordinates (x, y, w, h) and other losses. λ_{noobj} denotes the balancing parameter for the balance between the boxes with and without objects.

The neural network training for catheter and guidewire position tracking was conducted in an environment with a batch size of 64, momentum of 0.9, decay of 0.0005, and a learning rate of 1e-05. During the training process, 1600 data samples were used for training, and 402 samples were used for validation. A training and validation data set were randomly selected for each epoch. An NVIDIA Quadro M4 000 GPU was used for the learning process, and the code was implemented using TensorFlow (Version 1.8.0). The loss values based on the learning results are shown in Fig. 9. Based on the learning results, an RGB camera was installed on the vascular phantom. The resulting image of the catheter and guidewire position-tracking algorithm is shown in Fig. 10.

3.4 Reinforcement learning for autonomous surgical tools control

In this study, reinforcement learning was applied to the VIR robot for the autonomous VIR procedure. Reinforcement learning is a method of learning through trial and error. The reinforcement learning agent determines the action and the state changes through the action. Then, the environment calculates a reward value based on the reward function according to the state. The environment also provides to the agent the calculated reward value. The goal of reinforcement learning is to enable the agent to learn in a manner that realizes the maximum reward from the environment. Therefore, the state, reward, action, environment, and agent

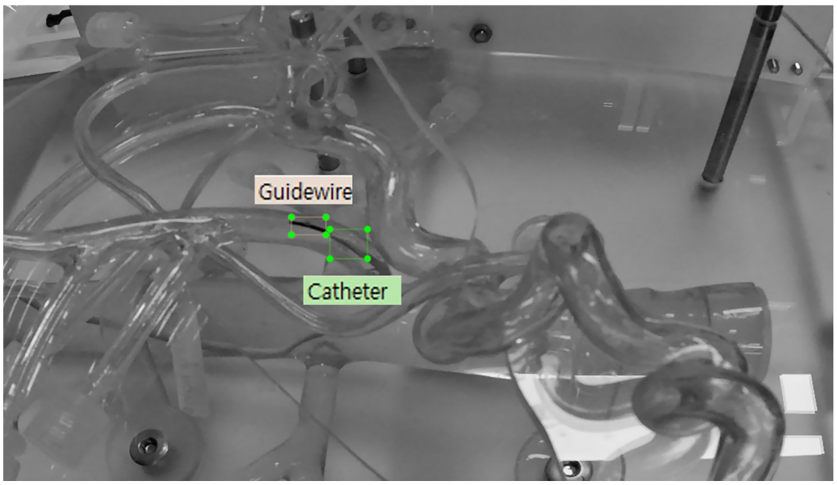

(a)


```
- <annotation>
    <folder>datasetandlabel</folder>
    <filename>SING0182.JPG</filename>
  - <source>
      <database>Unknown</database>
    </source>
  - <size>
      <width>5120</width>
      <height>3840</height>
      <depth>1</depth>
    </size>
    <segmented>0</segmented>
  - <object>
      <name>Guidewire</name>
      <pose>Unspecified</pose>
      <truncated>0</truncated>
      <difficult>0</difficult>
    - <bndbox>
        <xmin>1759</xmin>
        <ymin>1291</ymin>
        <xmax>1925</xmax>
        <ymax>1376</ymax>
      </bndbox>
    </object>
  - <object>
      <name>Catheter</name>
      <pose>Unspecified</pose>
      <truncated>0</truncated>
      <difficult>0</difficult>
    - <bndbox>
        <xmin>1944</xmin>
        <ymin>1349</ymin>
        <xmax>2125</xmax>
        <ymax>1491</ymax>
      </bndbox>
    </object>
</annotation>
```


(b)

Figure 8: Example of training data. (a) Grayscale image with bounding box label. (b) Bounding box label in extensible markup language format.

Figure 9: Learning graph for loss per learning time.

update methods are essential factors in reinforcement learning, and must be clearly defined for each component.

Figure 10 shows the reinforcement learning environment. The grayscale image size of the surgical tool position-tracking algorithm is 1920 × 1080 pixels. In reinforcement learning, the size of one state is defined as 60 × 60 pixels in the image. To visualize the reinforcement learning environment, each state is displayed in a grid pattern, as shown in Fig. 11. The state of reinforcement learning in this study is analogous to the catheter and guidewire positions in the image. An example of a state is defined in the environment, as shown in Equation (10), and the state is delivered to the reinforcement learning agent in the form of a tuple.

$$\text{state} = [\text{catheter X position, catheter Y position, guidewire X position, guidewire Y position}]. \quad (10)$$

Figure 11 shows the visualization of the reinforcement learning environment, the position of the surgical tools, and the target position.

The reward function used in reinforcement learning is defined in Equation (11) by modeling the process of the actual VIR procedure. In addition, the value of the F/T sensor was reflected in the reward function to reduce the repulsive force that may occur between the vascular phantom and catheter during the autonomous VIR procedure through reinforcement learning.

$$R = k_1 \cdot e^{-\sqrt{[(X_{go}-X_{gi})^2+(Y_{go}-Y_{gi})^2]}} + k_2 \cdot e^{-\sqrt{[(X_{go}-X_{ca})^2+(Y_{go}-Y_{ca})^2]}} + k_3 \cdot e^{-\sqrt{[(X_{gi}-X_{ca})^2+(Y_{gi}-Y_{ca})^2]}} - k_4 \cdot \log_{10}(\text{FT} - \text{sensorvalue}), \quad (11)$$

where X_{go} and Y_{go} denote the coordinates of x and y on the image of the target position, respectively. X_{gi}/Y_{gi} and X_{ca}/Y_{ca}, respectively, denote the x and y positions of the guidewire and catheter in the image coordinate system. FT − sensorvalue represents the value of the F/T sensor. If the F/T sensor value increases, the reward is defined as smaller, and it is finally reflected in the reward function through a logarithmic function. In this reward function, the distance between the target position and the surgical tools

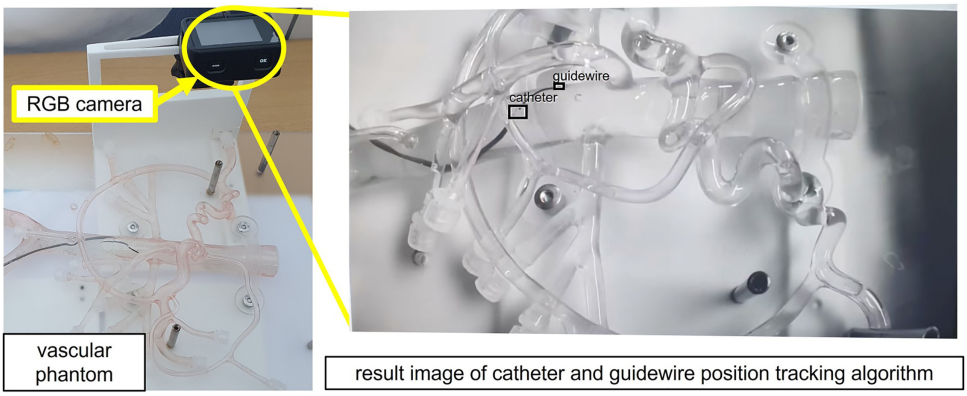

Figure 10: RGB camera installed on the vascular phantom and the resulting image of the catheter and guidewire position-tracking algorithm.

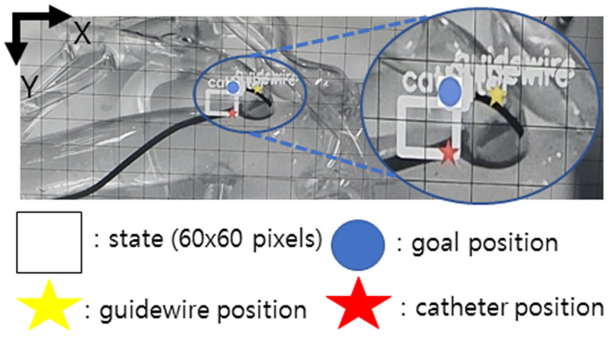

Figure 11: Visualization of the target position and the position of the surgical tools based on the defined state in the reinforcement learning environment.

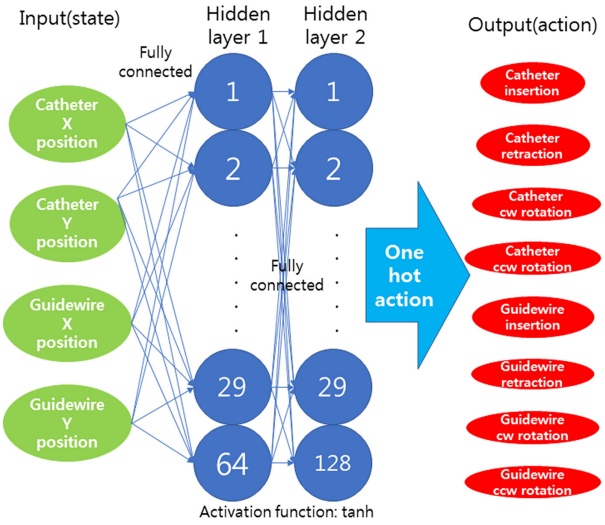

Figure 12: Schematic of a neural network in reinforcement learning.

was assigned a greater weight than the distance between the surgical tools and the value of the F/T sensor, such that k_1, k_2 were set to 0.3, and k_3, k_4 were set to 0.2.

The neural network used in reinforcement learning has two hidden layers. The first hidden layer consists of 64 nodes and the second hidden layer consists of 128 nodes. The activation functions of the two hidden layers were set as hyperbolic tangents. The input of the neural network is the state, which is the position of the catheter and guidewire, as shown in Equation (10). One of the VIR robot's eight actions that maximize the reward value is returned as the neural network output. Since the reward function is defined as Equation (11), the neural network can obtain a higher reward value as the surgical tools approach the target position and the F/T sensor value decreases. Figure 12 shows the structure of the neural network and the relationship between the input and output.

Mnih *et al.* (2015) presented the application of an experience replay buffer and fixed weights to increase learning efficiency in reinforcement learning. In this study, an experience replay buffer and fixed weights are applied to train the reinforcement learning algorithm more efficiently. The experience replay buffer data consist of [state, action, reward, next state, and next action]. The experience replay buffer used in the experiment contains 4 000 sets of experience replay data. We randomly selected 64 pieces of data from the experience replay buffer and updated the average of the losses with weights for every five learning steps. Training of the reinforcement learning algorithm was performed when the replay buffer was full, and 500 000 training iterations were performed.

4 Experiments

4.1 Experimental environment of the autonomous VIR robot

To verify the effectiveness of the deep learning algorithm applied to the autonomous VIR robot system, two types of phantoms are employed: abdominal and aortic arch. The target points of the vascular phantom were set, as shown in Fig. 13.

In this experiment, to maintain the characteristics of the VIR procedure, an experimental environment was built similar to the actual environment of the VIR procedure. As shown in Fig. 14, the catheter and guidewire position-tracking algorithm captured the vascular phantom through the RGB camera in only one location. This means that only the 2D image of the vascular phantom is provided to the surgical tool position-tracking algorithm in real time, similar to the X-ray image of the actual VIR procedure. An F/T sensor (RFT60-HA01, ROBOTOUS) was used to measure the repulsive force between the surgical tool and the vessel wall, which occurs during the procedure.

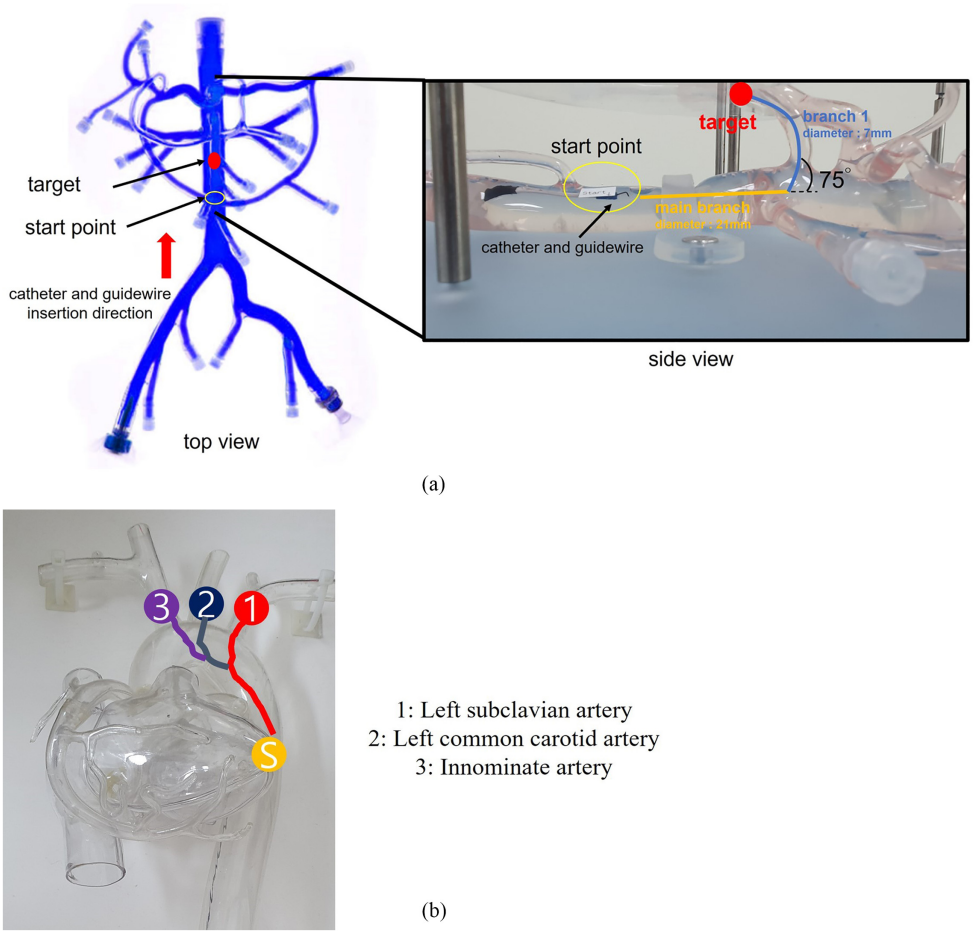

Figure 13: Target points for autonomous VIR procedure. (a) Target point of the abdominal vascular phantom. (b) Target points of the aortic arch vascular phantom.

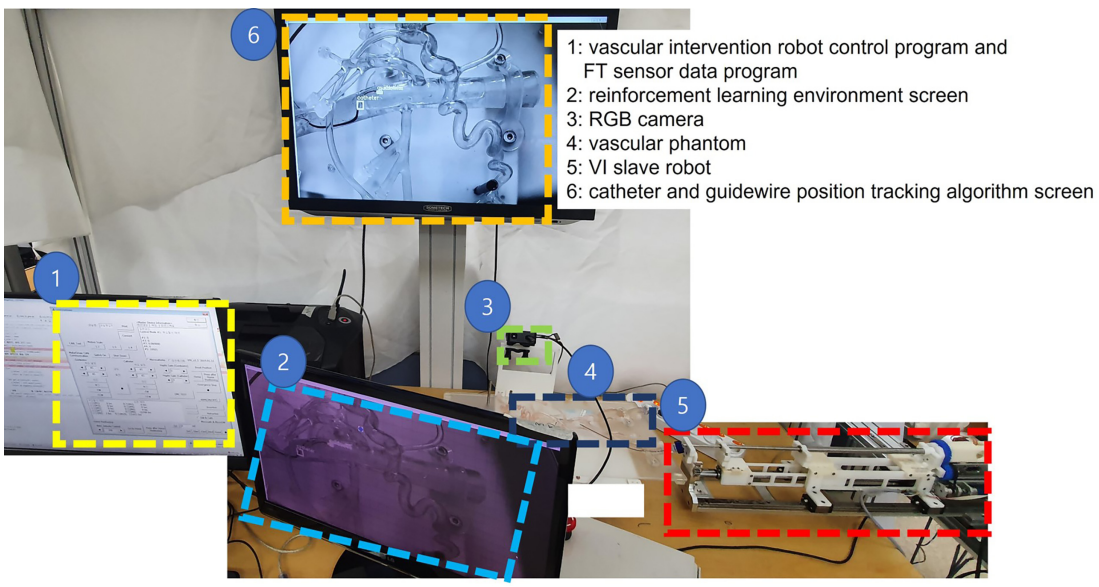

Figure 14: Experimental environment of the autonomous VIR robot.

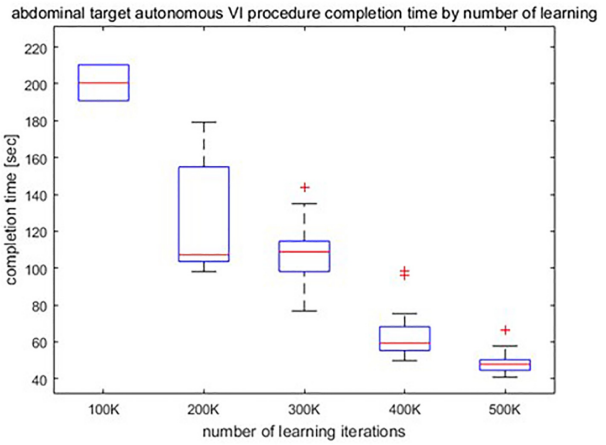

Figure 15: Variation in the abdominal target completion time of the autonomous VIR procedure with the number of learning iterations.

Table 2: Success rate of the autonomous VIR procedure according to the number of learning iterations (abdominal vascular phantom).

Number of learning iterations	Success rate
100 000	8%
200 000	36%
300 000	72%
400 000	92%
500 000	96%

4.2 Task-time and success rate of autonomous VIR procedure based on abdominal and aortic arch vascular phantoms

In the first experiment with an abdominal vascular phantom, a commercial 5 French 85 cm catheter (A&A M.D.) and 0.035 arcsec guidewire (Terumo) were used. We measure the task time of the autonomous VIR procedure and the success rate for each neural network training iterations. The task-time and success rate were measured 25 times for each training iteration. Figure 15 shows the task-time for each training iteration. Table 2 presents the success rate of the autonomous VIR procedure according to the number of learning iteration.

When the neural network was trained 100 000 times, the average task-time of the autonomous VIR procedure was measured at 200.6 s, and the measured success rate was 8%. When the number of learning iterations was 200 000, the measured average task-time was 125.2 s and the success rate was 36%. In the case of 300 000 learning iterations, the average task-time was 107.7 s and the success rate was 72%. For 400 000 training iterations, the average task-time was 63.9 s and the success rate was measured as 92%. Finally, for 500 000 training iterations, the average task-time was 48.3 s and the success rate was 96%. Training iterations in excess of 500 000 did not reduce the task time or increase the success rate.

In the second experiment with the aortic arch vascular phantom, a commercial straight type of 5 French 100 cm catheter and 0.035 arcsec guidewire were used. As in the case with the abdominal vascular phantom experiment, we measure the task-time of the autonomous VIR procedure and the success rate for each neural network training iterations. The task-time and success rate were measured 25 times for each training iteration. Figure 16

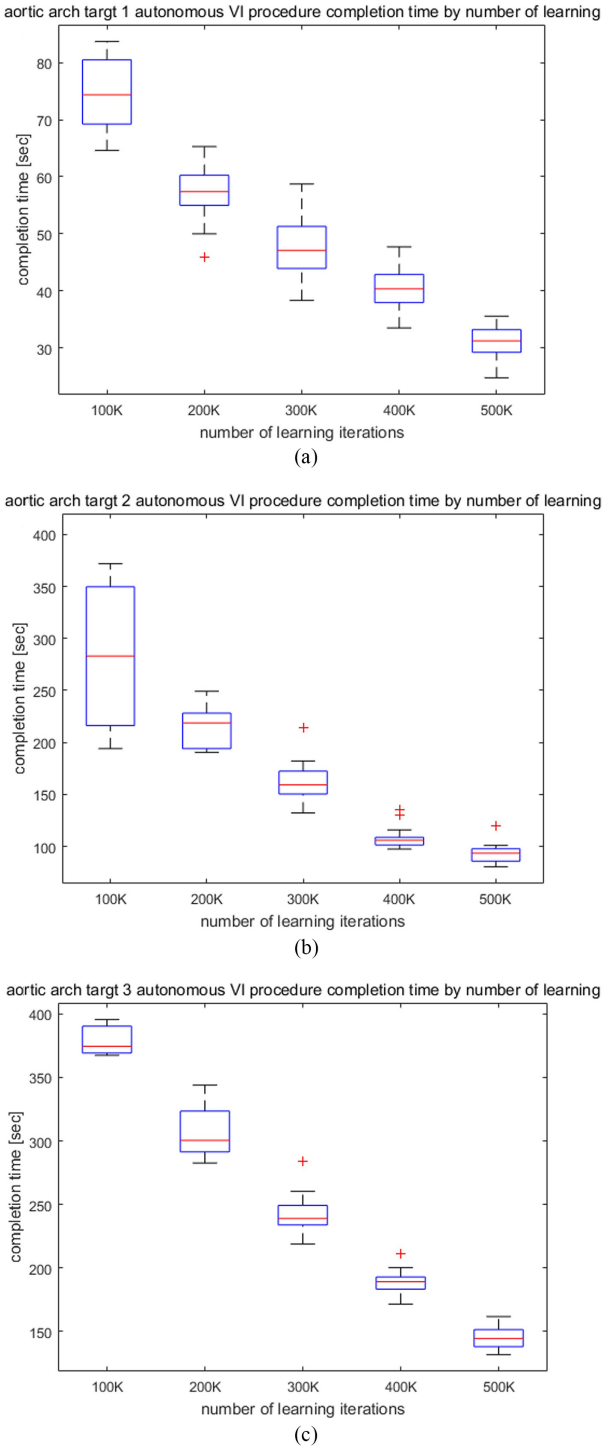

Figure 16: Variation of aortic arch target completion time of the autonomous VIR procedure with the number of learning iterations. (a) Target 1. (b) Target 2. (c) Target 3.

shows the task-time obtained for each training iteration. Table 3 presents the success rate of the autonomous VIR procedure according to the number of learning iteration. In addition, the statistical analysis result of task-time according to the number of learning iterations was $p < 0.001$.

For aortic arch target 1, when the neural network was trained 100 000 times, the average task-time of the autonomous VIR procedure was measured as 73.9 s, and the measured success rate

Table 3: Success rate of the autonomous VIR procedure according to the number of learning iterations (aortic arch vascular phantom).

Aortic arch target	Number of learning iterations	Success rate
1	100 000	52%
	200 000	84%
	300 000	92%
	400 000	100%
	500 000	100%
2	100 000	12%
	200 000	36%
	300 000	76%
	400 000	88%
	500 000	96%
3	100 000	8%
	200 000	24%
	300 000	72%
	400 000	88%
	500 000	96%

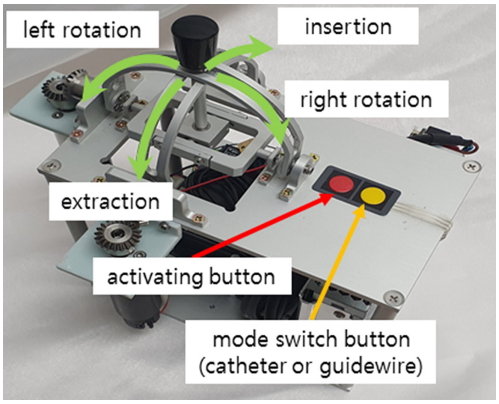

Figure 17: The two-DOF joystick structure master device of the master–slave VIR robot.

was 52%. When the number of learning iterations was 200 000, the measured average task-time was 57.5 s and the success rate was 84%. In the case of 300 000 learning iterations, the average task-time was 48.2 s and the success rate was 92%. For 400 000 training iterations, the average task-time was 40.4 s and the success rate was 100%. Finally, for 500 000 training iterations, the average task-time was 31.1 s and the success rate was 100%. Training iterations in excess of 500 000 did not reduce the task time or increase the success rate.

For aortic arch target 2, when the neural network was trained 100 000 times, the average task-time of the autonomous VIR procedure was measured as 282.9 s, and the measured success rate was 12%. When the number of learning iterations was 200 000, the measured average task-time was 215.6 s and the success rate was 36%. In the case of 300 000 learning iterations, the average task-time was 162.4 s and the success rate was 76%. For 400 000 training iterations, the average task-time was 108.6 s and the success rate was 88%. Finally, for 500 000 training iterations, the average task-time was 92.9 s and the success rate was 96%. Training iterations in excess of 500 000 did not reduce the task time or increase the success rate.

For aortic arch target 3, when the neural network was trained 100 000 times, the average task-time of the autonomous VIR procedure was measured as 379.1 s and the measured success rate was 8%. When the number of learning iterations was 200 000, the measured average task-time was 307.2 s and the success rate was 24%. In the case of 300 000 learning iterations, the average task-time was 241.8 s and the success rate was 72%. For 400 000 training iterations, the average task-time was 188.4 s and the success rate was 88%. Finally, for 500 000 training iterations, the average task-time was 144.5 s and the success rate was 96%. Training iterations in excess of 500 000 did not reduce the task time or increase the success rate. The statistical analysis result of task-time according to the number of learning iterations for all aortic arch targets was $p < 0.001$.

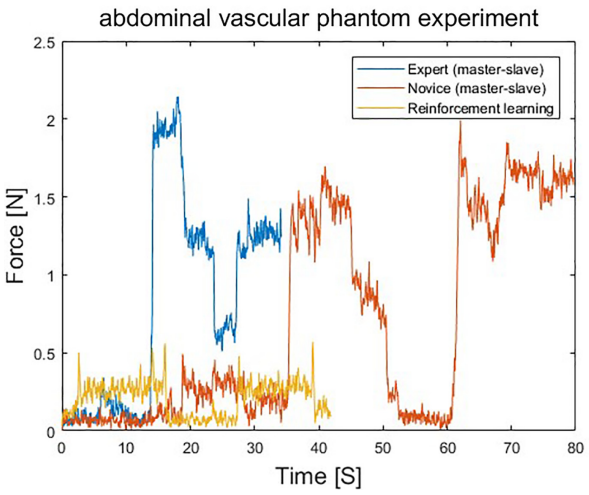

Figure 18: Repulsive force of abdominal vascular phantom for the master–slave VIR robot system and autonomous VIR robot system.

4.3 Comparison of the repulsive force between the autonomous VIR procedure and operator-driven master–slave VIR robot procedure

To verify the effect of reducing the repulsive force between the walls of the blood vessel and the surgical tool that occurs in the autonomous VIR procedure, an experiment was conducted using a master–slave robot system. However, unlike an autonomous VIR robot, the master–slave robot system allows the operator to manipulate surgical tools only through the master device. In the master–slave system operation, the operator is provided with only real-time 2D images installed in the vascular phantom, similar to the case of the autonomous VIR. The master device of the master–slave VIR robot system is a two-DOF joystick structure master device, as shown in Fig. 17.

In the first experiment with an abdominal vascular phantom master–slave VIR robot procedure, the repulsive force generated between the vessel wall and the surgical tool was measured. Three cases are compared in the experiment: the operator-driven master–slave method (novice and expert) and the autonomous VIR robot. Figure 18 presents one case of the experimental results of the repulsive force measurement of the master–slave VIR procedure and autonomous VIR procedure. For an expert operating the master–slave VIR procedure, the task-time was 38.2 s, the average force was 0.807 N, the maximum force was 2.259 N, and the total force over the entire operation time was 27.821 N. For a novice operating the master–slave VIR procedure, the task-time was 81.7 s, the average force was 0.675 N, the maximum force was

Table 4: Repulsive force of abdominal vascular phantom for master–slave VIR procedure and autonomous VIR procedure.

Type of VIR procedure	Average of repulsive force (N)	Maximum force (N)	STDEV force (N)	Total force (N∗Sec)
Master–slave VIR procedure (expert)	0.813	2.259	0.673	27.821
Master–slave VIR procedure (novice)	0.673	2.057	0.651	53.619
Autonomous VIR procedure	0.206	0.752	0.133	8.656

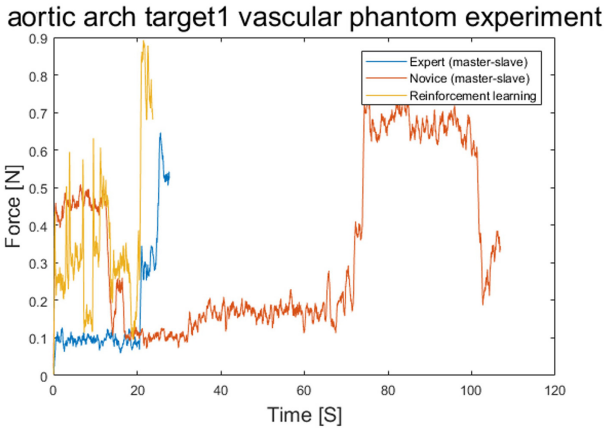

Figure 19: Repulsive force of aortic arch target 1 vascular phantom for the master–slave VIR robot system and autonomous VIR robot system.

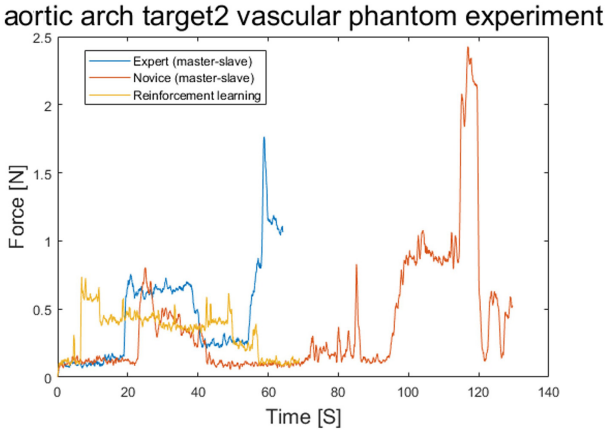

Figure 20: Repulsive force of aortic arch target 2 vascular phantom for the master–slave VIR robot system and autonomous VIR robot system.

2.057 N, and the total force over the entire operation time was 53.617 N. In the case of the autonomous VIR procedure, the task-time was 41.9 s, the average force was 0.206 N, the maximum force was 0.752 N, and the total force over the entire operation time was 8.656 N.

Compared to the master–slave VIR robot with the autonomous VIR robot operated by an expert, the autonomous VIR robot system reduced the average repulsive force by approximately 74%. Compared to the master–slave VIR robot with the autonomous VIR robot operated by a novice, the autonomous VIR robot system reduced the average repulsive force by approximately 69%. Meanwhile, the maximum force reduction effect of the autonomous VIR robot system was reduced by 65% compared with the master–slave VIR procedure.

Table 4 summarizes the results of the repulsive force measurement.

In the second experiment with the aortic arch target 1 vascular phantom master–slave VIR robot procedure, the repulsive force generated between the vessel wall and the surgical tool was measured. Figure 19 presents one case of the experimental results of the repulsive force measurement of the master–slave VIR procedure and the autonomous VIR procedure. For an expert operating the master–slave VIR procedure, the task-time was 27.7 s, the average force was 0.174 N, the maximum force was 0.872 N, and the total force over the entire operation time was 4.832 N. For a novice operating the master–slave VIR procedure, the task-time was 106.9 s, the average force was 0.336 N, the maximum force was 1.011 N, and the total force over the entire operation time was 35.927 N. In the case of the autonomous VIR procedure, the task-time was 23.7 s, the average force was 0.358 N, the maximum force was 1.091 N, and total force over the entire operation time was 8.511 N.

Compared to the master–slave VIR robot with the autonomous VIR robot obtained by an expert, the autonomous VIR robot system increased the average repulsive force by approximately 51%. Compared to the master–slave VIR robot with the autonomous VIR robot by novice, the autonomous VIR robot increased the repulsive force by 6%. In the expert case, the maximum force promotion of the autonomous VIR robot system was increased by 13% compared with the master–slave VIR procedure.

Table 5 summarizes the results of the repulsive force measurement.

In the aortic arch target 2 vascular phantom master–slave VIR robot procedure, the repulsive force generated between the vessel wall and the surgical tool was measured. Figure 20 presents one case of the experimental results of the repulsive force measurement of the master–slave VIR procedure and the autonomous VIR procedure. For an expert operating the master–slave VIR procedure, the task-time was 64.2 s, the average force was 0.456 N, the maximum force was 1.969 N, and the total force over the entire operation time was 29.301 N. For a novice operating the master–slave VIR procedure, the task-time was 129.6 s, the average force was 0.383 N, the maximum force was 2.593 N, and the total force over the entire operation time was 49.726 N. In the case of the

Table 5: Repulsive force of aortic arch target 1 vascular phantom for master–slave VIR procedure and autonomous VIR procedure.

Type of VIR procedure	Average of repulsive force (N)	Maximum force (N)	STDEV force (N)	Total force (N∗Sec)
Master–slave VIR procedure (expert)	0.174	0.872	0.167	4.832
Master–slave VIR procedure (novice)	0.336	1.011	0.234	35.927
Autonomous VIR procedure	0.358	1.091	0.214	8.511

Table 6: Repulsive force of aortic arch target 2 vascular phantom for master–slave VIR procedure and autonomous VIR procedure.

Type of VIR procedure	Average of repulsive force (N)	Maximum force (N)	STDEV force (N)	Total force (N∗Sec)
Master–slave VIR procedure (expert)	0.456	1.969	0.355	29.301
Master–slave VIR procedure (novice)	0.383	2.593	0.458	49.726
Autonomous VIR procedure	0.331	1.853	0.181	22.753

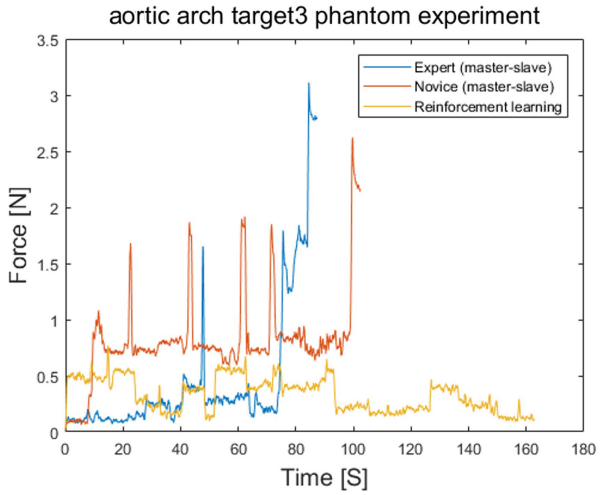

Figure 21: Repulsive force of aortic arch target 3 vascular phantom for the master–slave VIR robot system and autonomous VIR robot system.

autonomous VIR procedure, the task-time was 68.8 s, the average force was 0.331 N, the maximum force was 1.853 N, and the total force over the entire operation time was 22.753 N.

Compared to the master–slave VIR robot with the autonomous VIR robot operated by an expert, the autonomous VIR robot system reduced the average repulsive force by approximately 27%. Compared to the master–slave VIR robot with the autonomous VIR robot operated by a novice, the autonomous VIR robot system reduced the average repulsive force by approximately 13%. The maximum force reduction effect of the autonomous VIR robot system was reduced by 17% compared with the master–slave VIR procedure.

Table 6 summarizes the results of the repulsive force measurement.

In the aortic arch target 3 vascular phantom master–slave VIR robot procedure, the repulsive force generated between the vessel wall and the surgical tool was measured. Figure 21 presents one case of the experimental results of the repulsive force measurement of the master–slave VIR procedure and the autonomous VIR procedure. For an expert operating the master–slave VIR procedure, the task-time was 87.34 s, the average force was 0.469 N, the maximum force was 3.841 N, and the total force over the entire operation time was 40.989 N. For a novice operating the master–slave VIR procedure, the task-time was 102.39 s, the average force was 0.812 N, the maximum force was 3.125 N, and the total force over the entire operation time was 83.213 N. In the case of the autonomous VIR procedure, the task-time was 68.88 s, the average force was 0.331 N, the maximum force was 1.291 N, and the total force over the entire operation time was 53.775 N.

Compared to the master–slave VIR robot with the autonomous VIR robot operated by expert, the autonomous VIR robot system reduced the average repulsive force by approximately 29%. Compared to the master–slave VIR robot with the autonomous VIR robot operated by a novice, the autonomous VIR robot system reduced the average repulsive force by approximately 59%. The maximum force reduction effect of the autonomous VIR robot system was reduced by 62% compared with the master–slave VIR procedure.

Table 7 summarizes the results of the repulsive force measurement.

5 Discussion

The effectiveness of the autonomous VIR robot system based on a vascular phantom demonstrated a 96% success rate for the autonomous manipulation tool. In addition, the autonomous VIR robot system reduced the average repulsive force between the vessel wall and the surgical tool by 20–71% in all three targets except for the aortic arch target 1. In the case of the aortic arch target 1 experiment, the starting and the target points are arranged in a straight line, and it is relatively easy to access compared to other target points. Accordingly, in the case of aortic arch target 1, the measured force is smaller when the expert operator conducted the operation. On the other hand, the measured force is considerably large when the novice operator conducts the operation. In the proposed system, the maximum repulsive force of the experiment excluding the aortic arch target 1 tended to decrease from 6 to 66% compared to the expert-driven master–slave VIR robot system. The maximum repulsive force decreased from 28 to 63% compared to the novice-driven master–slave VIR robot system.

Reducing the maximum repulsive force is minimizing the vascular perforation during the VIR procedure. In addition, the proposed system decreased the standard deviation of the repulsive force from 49 to 80% compared to the case of expert -driven master–slave operation. In addition, the proposed system decreased the standard deviation of the repulsive force from 58 to 79% compared to the novice-driven master–slave operation. The low standard deviation of the repulsive force indicates that the autonomous VIR robot procedure exhibits less excessive movement than the master–slave VIR robot procedure. Except for the expert-driven master–slave operation for the aortic arch target 3

Table 7: Repulsive force of aortic arch target 3 vascular phantom for master–slave VIR procedure and autonomous VIR procedure.

Type of VIR procedure	Average of repulsive force (N)	Maximum force (N)	STDEV force (N)	Total force (N∗Sec)
Master–slave VIR procedure (expert)	0.469	3.841	0.648	40.989
Master–slave VIR procedure (novice)	0.812	3.125	0.416	83.213
Autonomous VIR procedure	0.331	1.291	0.171	53.775

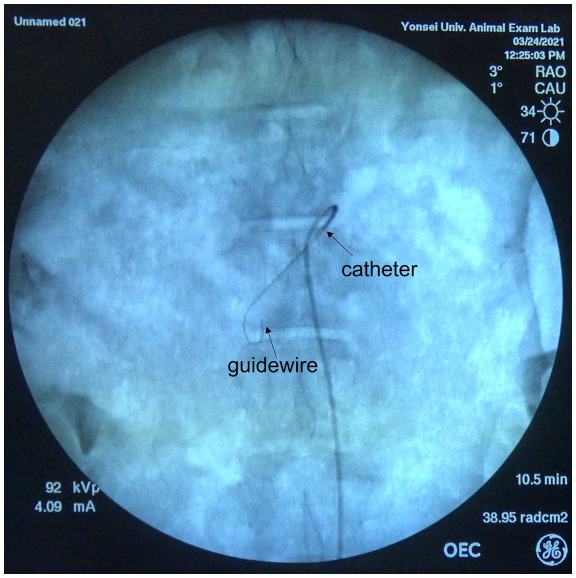

Figure 22: Example of in vivo VIR procedure X-ray image.

experiment, the autonomous VI robot system exhibited less repulsive force during the VIR procedure. For aortic arch target 3, the task completion time of the autonomous VIR robot system was prolonged because it was the most difficult target point to approach. Owing to the prolonged operation time, the total repulsive force of the procedure was larger than that of the expert-driven master–slave VIR robot system. The more difficult it is to approach the location, the greater is the difference in task completion time between the autonomous VIR robot system and the master–slave robot system. The more complex the vessels to access, the deeper the neural network should be applied to the autonomous VIR robot system to decrease the task completion time. For abdominal vascular target and aortic arch target 1, the proposed autonomous VIR robot was possible only with catheter manipulation. However, aortic arch targets 2 and 3 could not be accessed with a single guidewire or catheter manipulation, and autonomous vascular intervention was possible only with simultaneous manipulation.

However, the proposed autonomous VIR robot system still has many aspects to overcome: technical challenges, legal issues regarding the performance of autonomous surgery, and medical device certification for AI-based surgical robots. From a technical perspective, this study only showed the effectiveness based on the phantom, and the experiment was conducted using an RGB camera image rather than an X-ray image. If training of the surgical tool position-tracking algorithm is performed based on the X-ray image, it is expected that the surgical tool can be clearly identified on the X-ray image. However, in vivo experiments using pig models or humans will be more challenging than phantom-based experiments because not only the surgical tools and blood vessels, but also other body organs will appear in the screen as shown in Fig. 22. Moreover, in vivo experiments, injection of a contrast median is essential to display blood vessels on X-ray images. Future work will integrate remote drug injection equipment and the autonomous VIR robot system to overcome this limitation.

This research has been executed under the condition that the proposed autonomous VIR robot can only be applied when knowing the structure of blood vessels. In real clinical trial, each patient has its own blood vessel structure. To solve this problem, the agent must learn in a sophisticated simulation environment to enable autonomous manipulation of the surgical tool for the patient's blood vessel structure before the VIR procedure. Another limitation of the proposed autonomous VIR robot system is the need to set up a target position for each blood vessel branch. This limitation can be solved by applying the setting subgoal and final goal position method proposed by Kweon *et al.* (2021). In addition, the autonomous VIR robot system will become more complex because in vivo experiments must consider breathing motion. In future work compensation algorithm for breathing motion will be included. This research focuses only on the autonomous driving of the guidewire and catheter; additional research is needed on the intervention of additional surgical tools for blockage, rupture, or deformation of blood vessels. Also, there are still communication delays in the proposed autonomous VIR robot system while predicting the position of the surgical tool and making the tool movement decision. The proposed autonomous VIR robot system could not completely eliminate the delay because our system takes an average of 0.1 s to recognize the position of the surgical tool and determine the action. Also, in this study, the autonomous VIR procedure in 3D phantom model was conducted using only 2D image and F/T sensor data. We plan to conduct research using biplane X-rays for precise 3D surgical tool position control. Nevertheless, our future study will involve an animal experiment on pig models to verify the effectiveness of AI-based autonomous VIR robot systems and overcome these limitations.

Regarding the certification aspect of medical robots based on AI, as reported by Haidegger, the certification of commercialized medical robots has been approved by proving that they are equivalent to existing approved devices (Haidegger, 2019). For a newly developed surgical robot system to be certified as a medical robot that is not equivalent to an approved device, the certification period is five times longer, and the cost is over three times higher. Thus, it is necessary to publish international safety standards so that autonomous surgical robots can be equally certified as medical devices.

6 Conclusions and Future Works

This paper presents an autonomous VIR robot system based on deep learning algorithms, and its effectiveness was proven by performing vascular phantom-based experiments. The autonomous VIR robot system does not require the operator to control the master device; thus, the fatigue of the operator will be less than the master–slave VIR robot system. Furthermore, the autonomous VIR robot system will be free from communication delays caused by the limitation of the physical distance between the master device and slave robot. Furthermore, the autonomous VIR robot system learned to reduce the repulsive force between the vessel wall and the surgical tool, minimizing side effects such as vessel perforation. The experimental results of this research are conducted with respect to the abdominal and aortic arch vascular phantoms. Therefore, the autonomous VIR robot proves applicability to general VIR procedures. Based on the experimental results of a vascular phantom employing an autonomous VIR robot system, we believe that the autonomous VIR procedure can be applied in the near future as the autonomous VIR robot system will provide advantages for both patients and doctors.

Acknowledgments

This research was supported by the Basic Science Research Program through the National Research Foundation of Korea (NRF) funded by the Ministry of Education (2021R1I1A4A01051258).

Conflict of interest statement

The authors declare that there is no conflict of interest.

References

Advani, R., Naess, H., & Kurz, M. W. (2017). The golden hour of acute ischemic stroke. *Scandinavian Journal of Trauma, Resuscitation and Emergency Medicine*, **25**(1), 1–5. https://doi.org/10.1186/s13049-017-0398-5.

Anderson, P. L., Gelijns, A., Moskowitz, A., Arons, R., Gupta, L., Weinberg, A., & Kent, K. C. (2004). Understanding trends in inpatient surgical volume: Vascular interventions, 1980–2000. *Journal of Vascular Surgery*, **39**(6), 1200–1208. https://doi.org/10.1016/j.jvs.2004.02.039.

Bassil, G., Markowitz, S. M., Liu, C. F., Thomas, G., Ip, J. E., Lerman, B. B., & Cheung, J. W. (2020). Robotics for catheter ablation of cardiac arrhythmias: Current technologies and practical approaches. *Journal of Cardiovascular Electrophysiology*, **31**(3), 739–752. https://doi.org/10.1111/jce.14380.

Behr, T., Pusch, T. P., Siegfarth, M., Hüsener, D., Mörschel, T., & Karstensen, L. (2019). Deep reinforcement learning for the navigation of neurovascular catheters. *Current Directions in Biomedical Engineering*, **5**(1), 5–8. https://doi.org/10.1515/cdbme-2019-0002.

Boersma, E., Maas, A. C., Deckers, J. W., & Simoons, M. L. (1996). Early thrombolytic treatment in acute myocardial infarction: Reappraisal of the golden hour. *The Lancet*, **348**(9030), 771–775. https://doi.org/10.1016/S0140-6736(96)02514-7.

Britz, G. W., Panesar, S. S., Falb, P., Tomas, J., Desai, V., & Lumsden, A. (2019). Neuroendovascular-specific engineering modifications to the CorPath GRX Robotic System. *Journal of Neurosurgery*, **133**(6), 1830–1836. https://doi.org/10.3171/2019.9.JNS192113.

Cha, H. J., Yi, B. J., & Won, J. Y. (2017). An assembly-type master–slave catheter and guidewire driving system for vascular intervention. *Proceedings of the Institution of Mechanical Engineers, Part H: Journal of Engineering in Medicine*, **231**(1), 69–79. https://doi.org/10.1177/0954411916679328.

Cha, H. J., Yoon, H. S., Jung, K. Y., Yi, B. J., Lee, S., & Won, J. Y. (2016). A robotic system for percutaneous coronary intervention equipped with a steerable catheter and force feedback function. In *Proceedings of the 2016 IEEE/RSJ International Conference on Intelligent Robots and Systems (IROS)* (pp. 1151–1156). IEEE. https://doi.org/10.1109/IROS.2016.7759194.

Chareonthaitawee, P., Gibbons, R. J., Roberts, R. S., Christian, T. F., Burns, R., & Yusuf, S. (2000). The impact of time to thrombolytic treatment on outcome in patients with acute myocardial infarction. *Heart*, **84**(2), 142–148. http://dx.doi.org/10.1136/heart.84.2.142.

Chi, W., Dagnino, G., Kwok, T. M., Nguyen, A., Kundrat, D., Abdelaziz, M. E., & Yang, G. Z. (2020). Collaborative robot-assisted endovascular catheterization with generative adversarial imitation learning. In *Proceedings of the 2020 IEEE International Conference on Robotics and Automation (ICRA)* (pp. 2414–2420). IEEE. https://doi.org/10.1109/ICRA40945.2020.9196912.

Chi, W., Liu, J., Rafii-Tari, H., Riga, C., Bicknell, C., & Yang, G. Z. (2018). Learning-based endovascular navigation through the use of non-rigid registration for collaborative robotic catheterization. *International Journal of Computer Assisted Radiology and Surgery*, **13**(6), 855–864. https://doi.org/10.1007/s11548-018-1743-5.

Crinnion, W., Jackson, B., Sood, A., Lynch, J., Bergeles, C., Liu, H., & Booth, T. C. (2022). Robotics in neurointerventional surgery: A systematic review of the literature. *Journal of NeuroInterventional Surgery*, **14**(6), 539–545. http://dx.doi.org/10.1136/neurintsurg-2021-018096.

Duran, C., Lumsden, A. B., & Bismuth, J. (2014). A randomized, controlled animal trial demonstrating the feasibility and safety of the Magellan™ endovascular robotic system. *Annals of Vascular Surgery*, **28**(2), 470–478. https://doi.org/10.1016/j.avsg.2013.07.010.

Efstathopoulos, E. P., Pantos, I., Andreou, M., Gkatzis, A., Carinou, E., Koukorava, C., & Brountzos, E. (2011). Occupational radiation doses to the extremities and the eyes in interventional radiology and cardiology procedures. *The British Journal of Radiology*, **84**(997), 70–77. https://doi.org/10.1259/bjr/83222759.

Friedman, S. G. (2005). *A history of vascular surgery*. John Wiley & Sons.

Goni, H., Papadopoulou, D., Yakoumakis, E., Stratigis, N., Benos, J., Siriopoulou, V., & Georgiou, E. (2005). Investigation of occupational radiation exposure during interventional cardiac catheterisations performed via radial artery. *Radiation Protection Dosimetry*, **117**(1–3), 107–110. https://doi.org/10.1093/rpd/nci763.

Granada, J. F., Delgado, J. A., Uribe, M. P., Fernandez, A., Blanco, G., Leon, M. B., & Weisz, G. (2011). First-in-human evaluation of a novel robotic-assisted coronary angioplasty system. *JACC: Cardiovascular Interventions*, **4**(4), 460–465. https://doi.org/10.1016/j.jcin.2010.12.007.

Haidegger, T. (2019). Autonomy for surgical robots: Concepts and paradigms. *IEEE Transactions on Medical Robotics and Bionics*, **1**(2), 65–76. https://doi.org/10.1109/TMRB.2019.2913282.

Harel, G. (2021) The outcome of feasibility animal study. https://microbotmedical.com/wp-content/uploads/2021/09/Microbot-Investment-Presentation_HCW_-PDF.pdf. (25 July 2022, date last accessed).

Jeong, S., Chitalia, Y., & Desai, J. P. (2020). Design, modeling, and control of a coaxially aligned steerable (COAST) guidewire robot. *IEEE Robotics and Automation Letters*, **5**(3), 4947–4954. https://doi.org/10.1109/LRA.2020.3004782.

Karstensen, L., Behr, T., Pusch, T. P., Mathis-Ullrich, F., & Stallkamp, J. (2020). Autonomous guidewire navigation in a two dimensional vascular phantom. *Current Directions in Biomedical Engineering*, **6**(1). 20200007.

Karstensen, L., Ritter, J., Hatzl, J., Pätz, T., Langejürgen, J., Uhl, C., & Mathis-Ullrich, F. (2022). Learning-based autonomous vascular guidewire navigation without human demonstration in the venous system of a porcine liver. *International Journal of Computer Assisted Radiology and Surgery*, 1–8. https://doi.org/10.1007/s11548-022-02646-8.

Khan, E. M., Frumkin, W., Ng, G. A., Neelagaru, S., Abi-Samra, F. M., Lee, J., & Calkins, H. (2013). First experience with a novel robotic remote catheter system: Amigo™ mapping trial. *Journal of Interventional Cardiac Electrophysiology*, **37**(2), 121–129. https://doi.org/10.1007/s10840-013-9791-9.

Kweon, J., Kim, K., Lee, C., Kwon, H., Park, J., Song, K., & Kim, Y. H. (2021). Deep reinforcement learning for guidewire navigation in coronary artery phantom. *IEEE Access*, **9**, 166409–166422. https://doi.org/10.1109/ACCESS.2021.3135277.

Li, M. M., Hamady, M. S., Bicknell, C. D., & Riga, C. V. (2018). Flexible robotic catheters in the visceral segment of the aorta: advantages and limitations. *The Journal of Cardiovascular Surgery*, **59**(3), 317–321. https://doi.org/10.23736/s0021-9509.18.10458-7.

Lum, M. J., Rosen, J., King, H., Friedman, D. C., Lendvay, T. S., Wright, A. S., & Hannaford, B. (2009). Teleoperation in surgical robotics–Network latency effects on surgical performance. In *Proceedings of the 2009 Annual International Conference of the IEEE Engineering in Medicine and Biology Society* (pp. 6860–6863). IEEE. https://doi.org/10.1109/IEMBS.2009.5333120.

Ma, Y., Gogin, N., Cathier, P., Housden, R. J., Gijsbers, G., Cooklin, M., & Rhode, K. S. (2013). Real-time X-ray fluoroscopy-based catheter detection and tracking for cardiac electrophysiology interventions. *Medical Physics*, **40**(7), 071902. https://doi.org/10.1118/1.4808114.

Mahmud, E., Schmid, F., Kalmar, P., Deutschmann, H., Hafner, F., Rief, P., & Brodmann, M. (2020). Robotic peripheral vascular intervention with drug-coated balloons is feasible and reduces operator radiation exposure: Results of the robotic-assisted peripheral intervention for peripheral artery disease (RAPID) study II. *The Journal of Invasive Cardiology*, **32**(10), 380–384.

Miller, D. L., Balter, S., Cole, P. E., Lu, H. T., Schueler, B. A., Geisinger, M., & Anderson, J. (2003). Radiation doses in interventional radiology procedures: The RAD-IR study part I: Overall measures of dose. *Journal of Vascular and Interventional Radiology*, **14**(6), 711–727. https://doi.org/10.1097/01.RVI.0000079980.80153.4B.

Mnih, V., Kavukcuoglu, K., Silver, D., Rusu, A. A., Veness, J., Bellemare, M. G., Graves, A., Riedmiller, M., Fidjeland, A. K., Ostrovski, G., Petersen, S., Beattie, C., Sadik, A., Antonoglou, I., King, H., Kumaran, D., Wierstra, D., Legg, S., & Hassabis, D. (2015). Human-level control through deep reinforcement learning. *Nature*, **518**(7540), 529–533. https://doi.org/10.1038/nature14236.

Mohapatra, A., Greenberg, R. K., Mastracci, T. M., Eagleton, M. J., & Thornsberry, B. (2013). Radiation exposure to operating room personnel and patients during endovascular procedures. *Journal of Vascular Surgery*, **58**(3), 702–709. https://doi.org/10.1016/j.jvs.2013.02.032.

Mulder, M. J. H. L, Jansen, I. G. H., Goldhoorn, R.-J. B., Venema, E., Chalos, V., Compagne, K. C. J., Roozenbeek, B., Lingsma, H. F., Schonewille, W. J., van den Wijngaard, I. R., Boiten, J., Vos, J. A., Roos, Y. B. W. EM., van Oostenbrugge, R. J., van Zwam, W. H., Majoie, C. B. L. M., van der Lugt, A., & Dippel, D. W. J., MR CLEAN Registry Investigators. (2018). Time to endovascular treatment and outcome in acute ischemic stroke: MR CLEAN registry results. *Circulation*, **138**(3), 232–240. https://doi.org/10.1161/CIRCULATIONAHA.117.032600.

Pantos, I., Patatoukas, G., Katritsis, D. G., & Efstathopoulos, E. (2009). Patient radiation doses in interventional cardiology procedures. *Current Cardiology Reviews*, **5**(1), 1–11. https://doi.org/10.2174/157340309787048059.

Patel, T. M., Shah, S. C., Soni, Y. Y., Radadiya, R. C., Patel, G. A., Tiwari, P. O., & Pancholy, S. B. (2020). Comparison of robotic percutaneous coronary intervention with traditional percutaneous coronary intervention: A propensity score-matched analysis of a large cohort. *Circulation: Cardiovascular Interventions*, **13**(5), e008888. https://doi.org/10.1161/CIRCINTERVENTIONS.119.008888.

Redmon, J., Divvala, S., Girshick, R., & Farhadi, A. (2016). You Only Look Once: Unified, real-time object detection. In *Proceedings of the IEEE Conference on Computer Vision and Pattern Recognition*(pp. 779–788). IEEE. https://doi.org/10.1109/CVPR.2016.91.

Satiani, B., Williams, T. E., & Go, M. R. (2009). Predicted shortage of vascular surgeons in the United States: Population and workload analysis. *Journal of Vascular Surgery*, **50**(4), 946–952. https://doi.org/10.1016/j.jvs.2009.06.056.

Schanzer, A., Steppacher, R., Eslami, M., Arous, E., Messina, L., & Belkin, M. (2009). Vascular surgery training trends from 2001–2007: A substantial increase in total procedure volume is driven by escalating endovascular procedure volume and stable open procedure volume. *Journal of Vascular Surgery*, **49**(5), 1339–1344. https://doi.org/10.1016/j.jvs.2008.12.019.

Tahir, A., Iqbal, H., Usman, M., Ghaffar, A., & Hafeez, A. (2022). Cardiac X-ray image-based haptic guidance for robot-assisted coronary intervention: A feasibility study. *International Journal of Computer Assisted Radiology and Surgery*, **17**, 531–539. https://doi.org/10.1007/s11548-022-02563-w.

Vano, E., Gonzalez, L., Fernandez, J. M., Alfonso, F., & Macaya, C. (2006). Occupational radiation doses in interventional cardiology: A 15-year follow-up. *The British Journal of Radiology*, **79**(941), 383–388. https://doi.org/10.1259/bjr/26829723.

Wáng, Y. X. J., De Baere, T., Idée, J. M., & Ballet, S. (2015). Transcatheter embolization therapy in liver cancer: An update of clinical evidences. *Chinese Journal of Cancer Research,* **27**(2), 96. https://doi.org/10.3978/j.issn.1000-9604.2015.03.03.

Weerakkody, R. A., Walsh, S. R., Cousins, C., Goldstone, K. E., Tang, T. Y., & Gaunt, M. E. (2008). Radiation exposure during endovascular aneurysm repair. *Journal of British Surgery*, **95**(6), 699–702. https://doi.org/10.1002/bjs.6229.

Woo, J., Song, H. S., Cha, H. J., & Yi, B. J. (2019). Advantage of steerable catheter and haptic feedback for a 5-DOF vascular intervention robot system. *Applied Sciences*, **9**(20), 4305. https://doi.org/10.3390/app9204305.

Wrixon, A. D. (2008). New ICRP recommendations. *Journal of Radiological Protection*, **28**(2), 161. https://doi.org/10.1088/0952-4746/28/2/R02.

You, H., Bae, E., Moon, Y., Kweon, J., & Choi, J. (2019). Automatic control of cardiac ablation catheter with deep reinforcement learning method. *Journal of Mechanical Science and Technology*, **33**(11), 5415–5423. https://doi.org/10.1007/s12206-019-1036-0.